Journal of Materials Chemistry A

Accepted Manuscript

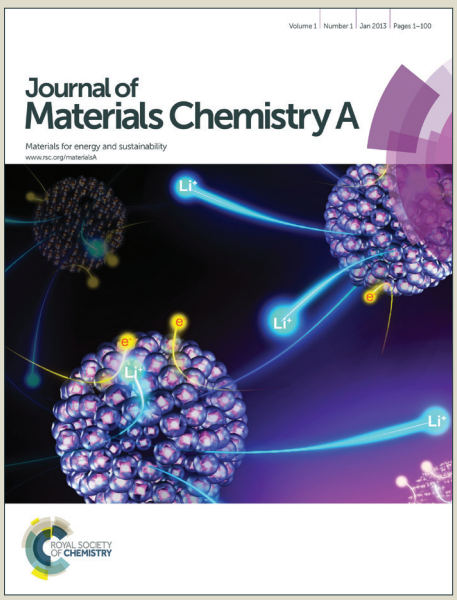

ROYAL SOCIETY OF CHEMISTRY

www.rsc.org/materialsA

Cite this: DOI: 10.1039/c0xx00000x

www.rsc.org/xxxxxx

ARTICLE TYPE

From Melamine-Resorcinol-Formaldehyde to Nitrogen-Doped Carbon Xerogels with Micro- and Meso-pores for Lithium Batteries

Xichuan Liu,[a] Shaomin Li,[a] Jun Mei,[a] Woon-Ming Lau,[a] Rui Mi,[a] Yinchuan Li,[a] Hao Liu,*[a] and Limin Liu[b]

Received (in XXX, XXX) Xth XXXXXXXXX 20XX, Accepted Xth XXXXXXXXX 20XX
DOI: 10.1039/b000000x

Novel multi-scaled porous nitrogen-doped porous carbon is synthesized by enriching the simple resorcinol-formaldehyde xerogels method with: (a) addition of melamine for nitrogen-doping and micron-duct formation; (b) incorporation of PEO-PPO-PEO micelles for the optimization of the duct percolation; and (c) integration of CO_2-etching to the carbonization process for the formation of abundant 2nm-pores. Our experimental results confirm that these nitrogen-doped carbon xerogels (NCXs) indeed comprise a multi-scaled porous structure having nano-porous carbon in a network of micron-size percolated hallow-channels. NCXs prepared with CO_2-etching at 950°C for 8 hours have a high surface area of 2912 m^2 g^{-1}. In addition, the lithium ion batteries fabricated with these NCXs show a high specific capacity of 645 mAh g^{-1}, with excellent cycle stability and good rate capability.

1. Introduction

Carbonaceous materials with hierarchical multi-scaled porosity have emerged as a family of outstanding functional materials with attractive properties such as high surface area, good thermal and chemical stability, and adequate electrical conductivity. These properties have been exploited with good success, and such porous carbon has been used to fabricate electrodes of chemical batteries[1, 2] and supercapacitors,[3, 4] adsorbents and storage materials,[5] and fuel-cell electrodes[6] and catalyst supports.[7] In these applications, nano-pores are typically the very key structural element for maximizing the effective surface area of the functional porous carbon; but well percolated micron-scaled pores are also desirable for fast transportation of reactants to translate surface reactions in the nano-pores to functional performance of the porous carbon. The most common, practical and inexpensive chemical method of fabricating functional porous carbon with nano-pores is carbonization of an organic gels having an adequate mixture of carbon and oxygen atoms in the molecular framework of the gels. In fact, phenol-based organic gels prepared by the polycondensation of resorcinol (R) and formaldehyde (F)[8] are now widely used as precursors of porous carbon. By adjusting the preparation procedures of this seemingly simple polycondensation process, one can produce porous carbon with pore-size varying from a few microns to a few nanometers.

Recently there have been two breakthroughs in further advancing this R-F route of porous carbon. The first breakthrough[9] makes use of uniform micelle formation of co-polymer having polyethylene-oxide (PEO), polypropylene-oxide (PPO), and PEO in a tri-block form, with the micelle conformation and size controlled by the molecular weight of the "block" units and by the micelle formation conditions. By coupling the PEO-PPO-PEO micelle formation to the R-F route, one can synthesize a new organic gel with PEO-PPO-PEO micelles embedded in a R-F gel which can prevent the severe volume shrinkage of the organic gel during the drying process of a typical R-F gel application. During carbonization, the oxidative annihilation of the oxygen-rich PEO-PPO-PEO micelles gives rise to an almost independent pore formation mechanism in parallel to the porous carbon formation derived from the R-F gel matrix.[10] In the other intriguing breakthrough,[11] carbonization in the presence of CO_2 as a weak oxidant and thus mild carbon-etchant is now known factually to be effective in generating pores of about 2nm in size in carbonaceous carbon. In short, novel carbonaceous materials with hierarchical multi-scaled porosity are flourishing with a combination of these new chemical designs and synthetic methods.

On the other hand, doping carbonaceous carbon with nitrogen is now known to have many attractive functional properties.[12-19] For instance, nitrogen-doping can provide more active sites for interface electrochemical reactions.[12] In addition, nitrogen-doping is also known to introduce a large number of surface defects that further enhances lithium intercalation properties.[13, 14] Further, in the energy-storage applications, due to improvement of electrochemical reactivity and electrical conductivity, nitrogen-doping of carbonaceous electrodes has been found to improve long-term electrochemical stability in lithium ion batteries and cycling performance in supercapacitors.[15] Recently, in their studies investigating the effects of nitrogen-doping of carbonaceous materials, Geng, et al.[16] and Zhong, et al.[17] postulate that nitrogen bonding configuration, textural structure, and surface area are critically important. Conversely, the amount of nitrogen incorporation turns out to be less important. In fact, Geng, et al.[16] pointed out that using nitrogen to substitute a

carbon atom in a perfect graphitic molecular sheet, with the resultant nitrogen atom having the quaternary nitrogen chemical configuration, is the most effective in enhancing the electrochemistry of oxygen reduction. However, clarification on why this is the case is lacking.

Further, recent studies have reported on new methods of doping carbonaceous materials with nitrogen. For example, Jin, et al. reported[18] that by adding cobalt nitrate as a nitrogen-dopant and polycondensation catalyst in the R-F route of porous carbon synthesis, one can make a new family of nitrogen-doped porous carbon. Furthermore, Zhong et al. showed[17] that carbonization of M-R-F gels with melamine partial replacing resorcinol in common R-F gels can also yield functional nitrogen-doped porous carbon. Such nitrogen-doped porous carbon has been shown to be effective in facilitating oxygen-reduction-reaction (ORR) whereas porous carbon with no nitrogen-doping carries no such functional property[19]. However, these two innovations focus on nitrogen doping, with no consideration of pore structure design.

Herein we synthesize and characterize nitrogen-doped carbon xerogels (NCXs) with hierarchical multi-scaled porosity by incorporating the following design considerations to address both effective nitrogen doping and pore-structure formation:

1. A stimulating set of new result by Zhou et al. on molecular conformation of M-R-F co-polycondensates shows that R-rich phases and M-rich phases are intermixed microscopically.[20] It is now also known that carbonization of an M-F gels yields pores due to nitrogen and carbon loss, with the N/C atomic ratio changed from the original 5/3 in M to a few atomic % in the resultant porous carbon xerogels. We combine these two features into forming a nitrogen-doped porous carbon with nano-scaled pores derived from the R-rich phase of the M-R-F gels and with additional percolated porous channels, about a micron in size, derived from the M-rich phase.
2. We further adopt the PEO-PPO-PEO micelle method, to stabilize the M-R-F gels and to instrument a porous structure with micron-channels, about a few microns in size so as to, facilitate transport of reactants into the M-R-F derived porous carbon with micron-channels and nano-pores.
3. Finally, we adopt the carbon dioxide assisted carbonization method to add abundant 2nm-pores in the nitrogen-doped carbonaceous materials with hierarchical multi-scaled porosity derived from the R-M-F/PEO-PPO-PEO-micelle gels.
4. We use the resultant nitrogen-doped xerogels with multi-scaled micro- and meso-pores as anode of lithium ion battery, and study the effects of nitrogen-doping.

Incorporating these diverse methods into the synthesis process is a novel approach.

2. Experimental

2.1 Chemicals

Resorcinol, formaldehyde and NaOH were purchased from Kelong Chemical reagent Co. (Chengdu, China); Melamine and polyvinylidene fluoride (PVDF) was purchased from Sinopharm Chemical Reagent Co. (Shanghai, China); F68 was purchased from Sigma-Aldrich. All the reagents were used without further purification. Deionized water was used in all experiments.

2.2 Sample preparation

NCXs were prepared by a sol-gel reaction from a solution containing R, F and M, followed by aging, solvent exchange, drying and pyrolysis. In this process, the ration of R and F was fixed at 2:1. Meanwhile, an extra amount of F was added with M in the ratio of 4:1 (M: F). F68 (PEO_{76}-PPO_{29}-PEO_{76}), was firstly dissolved in a small amount of ethanol at 60 °C. Then all reagents (R, M and F) were added to the solution. NaOH solution (0.02 mol L^{-1}) was employed to catalyze this sol-gel reaction and the molar ration of (R+M) to NaOH was determined at 100. The mixture was stirred at 60 °C until the solution became clear. Subsequently, the mixture was transferred to a sealed container and kept at 60 °C for 72h to complete the gel process. The resultant M-R-F hydrogels containing PEO_{76}-PPO_{29}-PEO_{76} were soaked in a solution of trifluoroacetic acid and ethanol (3:97 in volume) at room temperature for 72h. Afterwards, the residual solvent was replaced with fresh ethanol every 24 hours for 6 times to remove water thoroughly from the MRF hydrogels. Although, both the aging and solvent exchange steps were conducted at ambient conditions, the sample maintained its size without shrinkage. Subsequently, the obtained M-R-F hydrogels were dried at 60°C at ambient conditions. The wet organic gels preserved their cylindrical shape but were reduced from $\pi\times(16.4)^2\times59.5$ mm^3 to $\pi\times(15.5)^2\times59.0$ mm^3 after drying, a measurement which showed nearly negligible volume shrinkage due to the application of F68 which could steady the gel skeleton. Subsequently, the prepared organic M-R-F gels were carbonized in a tubular furnace with argon flow rate of 150 mL min^{-1} at a temperature of 800°C for 4h to form NCXs. In the final carbon dioxide activation process, to activate NCXs with large surface area and excessive pore volume, the NCXs were heated in a tubular furnace from room temperature to desired temperatures with a heating rate of 10°C min^{-1} in vacuum for a certain time (Table 1) under a steady carbon dioxide flow of 150 mL min^{-1}. For comparison, CXs were prepared by a similar process except for the addition of melamine.

Table 1 The temperature and times of carbon dioxide activation.

Sample	NCXs900-4	NCXs950-4	NCXs950-6	NCXs950-8
T / °C[a]	900	950	950	950
t / hour[b]	4	4	6	8

[a] T is the carbon dioxide activation temperature. [b] t is the carbon dioxide activation times.

2.3 Characterization of the multi-scaled porous NCXs

The morphology of the multi-scaled porous NCXs was observed by scanning electron microscopy (SEM) and high-resolution transmission electron microscopy (HRTEM). Raman spectroscopy measurements were carried out with a home-built Raman spectroscopy instrument. N_2 adsorption and desorption isotherms were conducted with an AUTOSORB-1 surface area analyzer (Quantachrome Instrument Corporation) at 77K. Specific surface areas were determined by the Brunauer-Emmett-Teller (BET) method and the non-local density functional theory (NLDFT) program was employed to estimate the pore size distribution. The chemical composition of the multi-scaled porous

NCXs was analyzed by X-ray photoelectron spectroscopy (XPS).

2.4 Electrochemical measurements

Electrochemical experiments were carried out in a CR2032-type coin cell. The working electrodes were prepared by mixing 80 wt% active materials, 10 wt% acetylene black, and 10 wt% PVDF in N-methylpyrrolidinone (NMP) to form a homogenous slurry. The slurry was then spread on a copper foil current collector. Afterwards, the electrode was dried overnight in a vacuum oven to eliminate the remaining solvents. Coin cells were assembled in an argon-filled glove box with both oxygen and moisture content lower than 0.1 ppm. A typical cell comprised lithium metal as the counter electrode, a polypropylene (PP, Cellgard 2500) film as separator, and 1 mol L^{-1} solution of $LiPF_6$ in ethylene carbonate (EC) and dimethyl carbonate (DMC) (1:1 in volume) as electrolyte. After the cells were aged for 24h, galvanostatic charge/discharge tests, cycling performance and rate capability were performed at a voltage ranging from 0.01 to 3 V by an ARBIN cell test instrument. Cyclic voltammetry (CV) was performed in the same range at a scanning rate of 0.1 mV s^{-1} by a PARSTAT 4000 electrochemical workstation. Electrochemical impedance spectroscopy (EIS) measurements were carried out in the frequency range from 100 kHz to 100 mHz.

Results and Discussion

From studies about R-F gel formation,[8] it is known that the major reactions between R and F include an addition reaction to form hudroxymethyl derivatives (-CH_2OH), and a condensation reaction of the hudroxymethyl derivatives to form methylene (-CH_2-) and methylene ether (-CH_2OCH_2-) bridged compounds. Similar sol-gel reactions between M and F were also observed in other study.[21, 22] In this work, we found that gel formation with a mixture of M-R-F was also effective. More importantly, we confirmed that integrating the PEO-PPO-PEO micelle strategy into the M-R-F gel formation can lead to stabilization of the M-R-F gels. This confirmation is deduced from our measurements of volume shrinkage during the gels drying process. In addition, we also found that the integration of the PEO-PPO-PEO micelle strategy into the M-R-F gel formation also offers one more way of fine tuning the porous structure of the resultant xerogel. More specifically, proper incorporation of the relative amount of PEO-PPO-PEO was found to add hallow-channels that enhance transport and diffusion, and to increase the presence of nano-pores for raising surface area.

Our hypothesis of xerogel formation mechanisms is depicted in scheme 1. Briefly, a condensation reaction occurs among the hydroxymethyl groups between M-F, and R-F to form methylene and methylene ether bridged polymers. They can then co-condense to form small clusters consisting of branched polymeric species. The small clusters act as nucleation sites which can continuously grow to form microspherical colloids. In parallel, some PEO-PPO-PEO micelles are entrapped within the growing colloids, which ultimately contribute to the formation of additional porosity.

The morphological and structural analysis of our xerogels is shown in the following figures. Fig. 1a shows carbon xerogels (CXs) with a 3D architecture comprising interconnected carbon

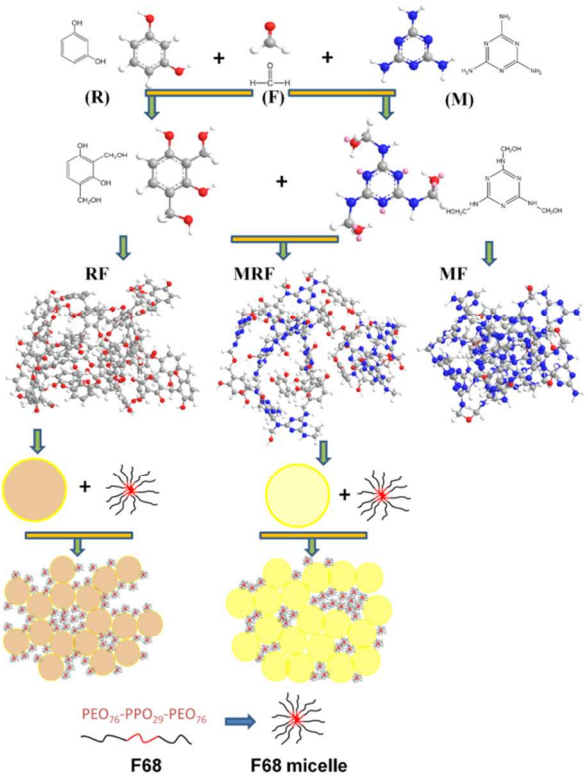

Scheme 1 Schematic representation of the preparation of R-F/ PEO-PPO-PEO-micelle gels and M-R-F/ PEO-PPO-PEO-micelle gels using ChemDraw.

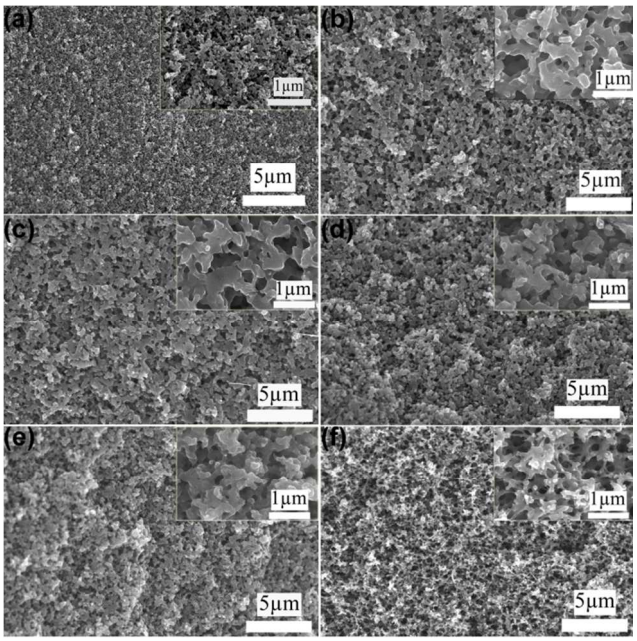

Fig. 1 SEM images of CXs (a) and multi-scaled porous NCXs (b, NCXs without CO_2 activation; c, NCXs900-4 activated at 900 °C for 4 hours; d, NCXs950-4, e, NCXs950-6, and f, NCXs950-8 which activated at 950°C for 4, 6, 8 hours, respectively).

spheres, and interconnected hallow-channels of 100-200 nm in size derived from the decomposition of PEO-PPO-PEO-micelle.[9, 23] Furthermore, enriching the R-F/ PEO-PPO-PEO-micelle gels with the addition of M gives a new pore structure: percolated

hallow-channels of about one micron in size (Fig. 1b). Because of the decomposition of M-F clusters and PEO-PPO-PEO-micelles, the NCXs (Fig. 1b) display a foam-like microstructure with many internal interconnected porous structures.[10, 24] After carbon dioxide activation at 900 °C for 4 hours (Fig. 1c), the overall structure morphology, as revealed by SEM imaging, hardly changed compared with that of NCXs without activation. When the activation temperature was increased to 950 °C, reduction of the primary carbon particle size is evident, as shown in Figs 1d, e, and f. One would expect that when the carbon dioxide activation temperature is raised, the oxidative activity of carbon dioxide towards etching carbon also increases.[25] In summary, the examination of NCXs with different activation durations reveals that all these NCXs present a similar foam-like structure except that the carbon skeleton becomes thinner and the size of primary carbon particle further decreases with the lengthening of activation period. This phenomenon is especially obvious in Fig. 1f which shows that an activation duration of 8 hours led to the formation of NCXs comprising carbon nanoparticles of less than 100 nm in diameter. This phenomenon is reasonable because considering the etching effect, longer activation duration could lead to more carbon loss.

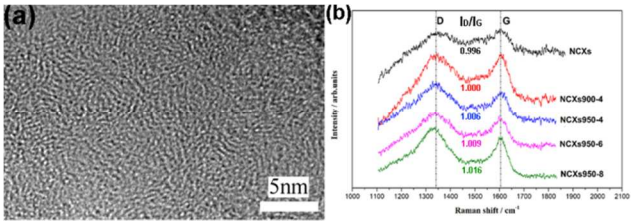

Fig. 2 The HRTEM of NCXs950-8 (a) and the Raman spectra of multi-scaled NCXs (b).

Activation of carbon xerogels by sintering in CO_2 is known to produce nano-size meso-pores of 2-3nm in diameter [25, 26] but obviously the formation of such nano-size features are not detectable in SEM images such as those in Fig.1a - f. To examine such changes, we turned to HRTEM imaging. Fig. 2a reveals that many nano-size meso-pores are abundant within NCXs and the NCXs structure is basically amorphous in nature, with sp^2 carbon derived mainly from the phenolic precursor randomly aggregates molecularly. Moreover, Raman spectra of multi-scaled porous NCXs (Fig. 2b) display the two prominent broad peaks typically found in carbonaceous materials, with the D band around 1350 cm^{-1} and the G band around 1600 cm^{-1}. The D band intensity is generally related to sp^3-related structural defects and disordered features of graphitic carbon, while the G band is the finger-print of graphitic crystallites of carbon.[27] The presence of both D and G bands are found in many disordered graphitic carbonaceous materials.[28, 29] The intensity ratio of I_D/I_G is the parameter routinely used to clarify the relative concentration of sp^3/sp^2 carbon, and to analyze defective structures in graphite-like materials. In our work, this ratio grows slightly with increasing activation temperature and duration (Fig. 2b). The relative increase of the D-band implies a loss of the perfect sp^2 structure of graphite (origin of the G-band) and a yield of defective graphite and other sp^3-like carbon strctures (origin of the D-band). Hence, the overall structure comprises graphite grains with an increasing amount of structural defects formed during the CO_2 activation. The result is consistent with the high-resolution TEM results on NCXs which show the presence of an amorphous carbon structure with localized nano-carbon-grains having planar-spacing close to that of graphite.

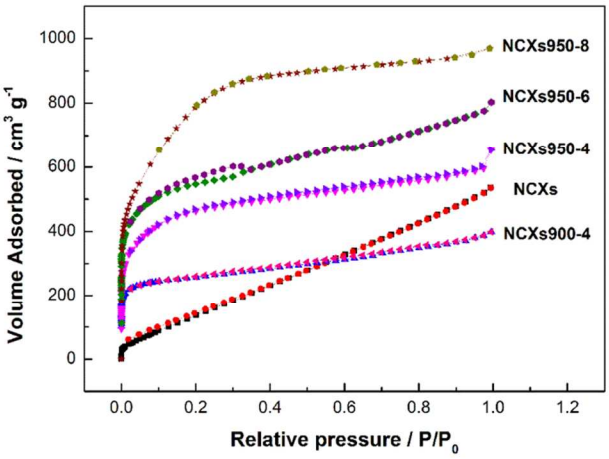

Fig. 3 Nitrogen adsorption/desorption isotherms of the multi-scaled porous NCXs.

To further examine the porous structure of the multi-scaled porous NCXs, nitrogen adsorption/desorption isotherms were measured at 77 K, as shown in Fig. 3. Additional data about pore size distributions of NCXs are included in Fig. S1. Relevant pore properties including BET surface area, average pore diameter, and total pore volume are summarized in Table 2. In brief, the isotherm data support that the carbon dioxide activation process is effective in promoting adsorption, as shown in Fig.3 As also shown in Fig.3, the adsorption curves of NCXs do not coincide with their desorption counterparts, but the differences are little. This kind of isotherms can be classified as Type IV by IUPAC,[30] characteristic of mesoporous materials. The hysteresis differences are of Type H4, indicating the presence of slit-shaped pores. This result can be confirmed by the pore size distributions shown in Fig. S1a. After carbon dioxide activation, distinct changes occurred from the isotherms as can be seen from the sharp rise at low relative pressure and the increase in the adsorbed amount. All the isotherms of activated NCXs exhibit some characteristics of Type I behavior designating the presence of micropores and Type IV behavior designating the presence of mesopores (Fig. 3),[30, 31] as shown in Fig. S1.

Table 2 Relevant parameters for the pore properties determined by nitrogen adsorption and desorption isotherms.

Sample	S_{BET} / (m^2 g^{-1}) [a]	w / (nm) [b]	V_t / (cm^3 g^{-1}) [c]
NCXs	744	4.4	0.83
NCXs900-4	982	2.5	0.90
NCXs950-4	1732	2.3	1.10
NCXs950-6	2137	2.2	1.24
NCXs950-8	2912	2.1	1.50

[a] S_{BET} is the specific surface area calculated from BET equation. [b] w is the average pore diameter. [c] V_t is the total pore volume.

As shown in Table 2, the specific BET surface area of NCXs with no CO_2 activation treatment is 744 m^2 g^{-1}. In comparison, the surface area increased to 981.9 after activation for 4 hours at 900 °C (Sample NCXs900-4). When the carbon dioxide activation was conducted at a temperature of 950 °C, more micro-/meso-

pores were created and the specific surface area of NCXs950-4, NCXs950-6 and NCXs950-8 increase to 1732, 2137 and 2912 $m^2 g^{-1}$, respectively. In addition, the total pore volume of NCXs and activated NCXs also increases with both activation temperature and time. In contrast, the average pore size of NCXs and activated NCXs were found to decrease with activation temperature and duration, with a value approaching 2nm. The results suggest that CO_2 activation tends to produce micro-pores with size below 2nm, particularly when activation is conducted at a relative high temperature of 950°C.

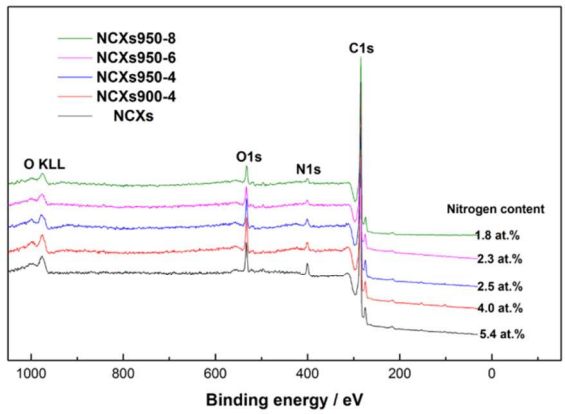

Fig. 4 XPS spectrum of the multi-scaled porous NCXs.

XPS was employed to characterize the composition and the nitrogen bonding environments of the multi-scaled porous NCXs. Both NCXs and activated NCXs exhibit three main groups of spectral peaks identified in the XPS spectra, corresponding to C1s, N1s and O1s, as shown in Fig. 4. The nitrogen contents present in the NCXs and activated NCXs, defined as atomic percent of nitrogen with respect to carbon, is estimated by the area ratio of the nitrogen and carbon peaks. It was found that the nitrogen content of NCXs was 5.4 at.%, which proves that nitrogen was incorporated into the carbon xerogels. After carbon dioxide activation for 4 hours at 900°C, the nitrogen content of the xerogel decreased to 3.9 at.%. The content decreased to 2.5 at.% when the activation temperature was changed to 950 °C. Increasing the activation time also led to further decrease of the nitrogen content. Only 1.8 at.% of nitrogen remained after an 8-hour carbon dioxide activation at 950 °C. This nitrogen content loss could be attributed to the fact that the reaction activities of nitrogen is higher than that of carbon in the reaction atmosphere of the CO_2 when activation treatments are performed at high temperature.[32]

Analysis of N1s spectra of the multi-scaled porous NCXs were carried out to evaluate the bonding environment and electronic structures of the nitrogen spices with the NCXs. There were three forms of nitrogen for every sample (Fig. 5) and all asymmetric N1s spectra of samples before and after activation could be deconvoluted into three spectral components at 398.5, 400.4 and 401.7 eV. This implies that all these samples have their residual nitrogen present in three bonding environments, and the CO_2 activation process does not induce the creation of any new chemical state of nitrogen. Among these three chemical states of nitrogen, the peak at around 398.5 eV is attributed to pyridinic-N,

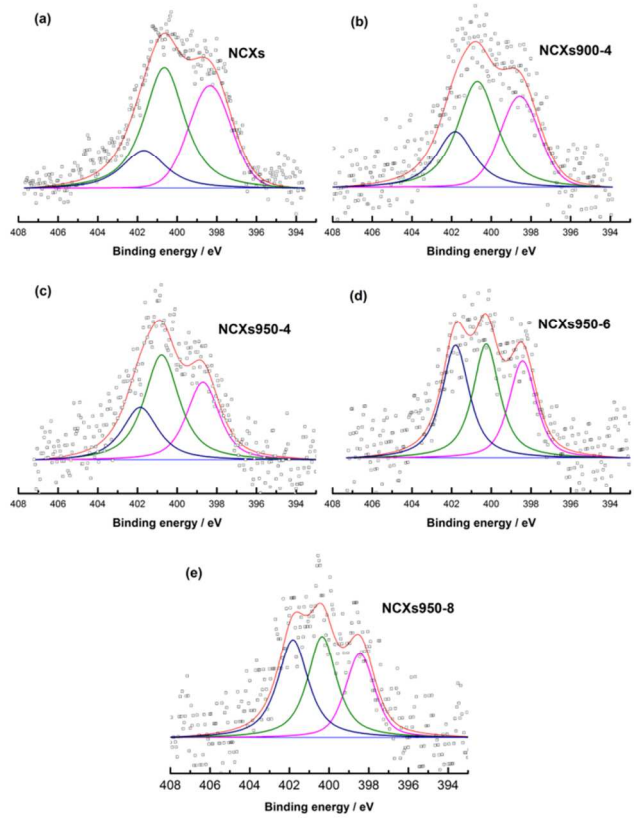

Fig. 5 XPS N1s spectra of the multi-scaled porous NCXs.

Table 3 Nitrogen forms of the multi-scaled porous NCXs from N1s XPS spectrum.

Sample	Nitrogen forms at.%[a]		
	pyridinic-N	pyrrolic-N	quaternary-N
NCXs	32.4	50.7	16.9
NCXs900-4	30.8	45.8	23.4
NCXs950-4	29.4	46.4	24.2
NCXs950-6	28.2	35.5	36.3
NCXs950-8	26.6	36.2	37.2

[a] The nitrogen forms contents are derived from N1s spectra.

which is equivalent to the neutral imine nitrogen of a triazine ring.[22] The peak at around 400.4 eV is ascribed to pyrrolic-N, corresponding to neutral amine nitrogen atoms.[22] Finally, the peak at around 401.7 eV is assigned to the quaternary-N, with nitrogen substituting carbon in a perfect graphitic sheet.[31] The relative content of each kind of nitrogen in all NCXs with and without activation are listed in Table 3. The results show a general trend of concentration reduction for both pyridinic-N and pyrrolic-N due to CO_2 activation. In contrast, the content of quaternary-N tends to increase with CO_2 activation. Since CO_2 activation also enhances the electrochemical performance of NCXs employed as anode in lithium ion battery, the correlation of quaternary-N and good electrochemical performance can be drawn. If this correlation is valid, the chemical state analysis of nitrogen in NCXs and the process designs towards increasing quaternary-N can be used as a practical strategy in developing high-performance M-R-F gels and NCXs, and their applications in lithium ion battery.

The chemical state analysis of carbon in NCXs was also performed and the results show that the C1s spectra for the multi-

scaled porous NCXs can be deconvoluted into five components: a component at around 284.5 eV indicating the presence of C-C bonds in graphitic carbon; a peak at around 285.3 eV indicating the presence of sp^3-like defects in the main graphitic structure of NCXs; peak at around 286.6 eV indication the presence of C-O or C-N species; and a spectral peak at 288.1 eV indicating the presence of C=O species. In addition, there is a very weak band at around 290 eV and this indicates the presence of carboxylic carbon. The spectral data are included in Fig. S2. The results and interpretations are consistent with those in the literature.[33]

The chemical state analysis of carbon shows the presence of some residual oxygen in the xerogels, which is indeed consistent with the detection of oxygen in the survey XPS scans shown in Fig. 4 and Fig. S3. The presence of residual oxygen is not surprising because oxygen is abundant in the precursor gels. During carbonization, most oxygen atoms are consumed by their oxidation reactions with carbon but some of them are expected to present in the resultant CXs or NCXs, for terminating and stabilizing carbon atoms at the edge-sites and defect sites of the carbonaceous body. Some of the detected residual oxygen may also be oxygen-containing species chemisorbed on CXs or NCXs due to the good absorbent nature of xerogels. Although residual oxygen is always present in NCXs, by comparing CXs (Table S1) and NCXs, we found no correlation between the presences of residual oxygen to the observed improvement of electrochemical performance of NCXs. Further, we also found no N-O species in NCXs. The claim is supported by the fact that, the presence of N-O species would give XPS spectral intensity in N1s at binding energy higher than 402eV; but for all NCXs in this work, such spectral components were not detected.

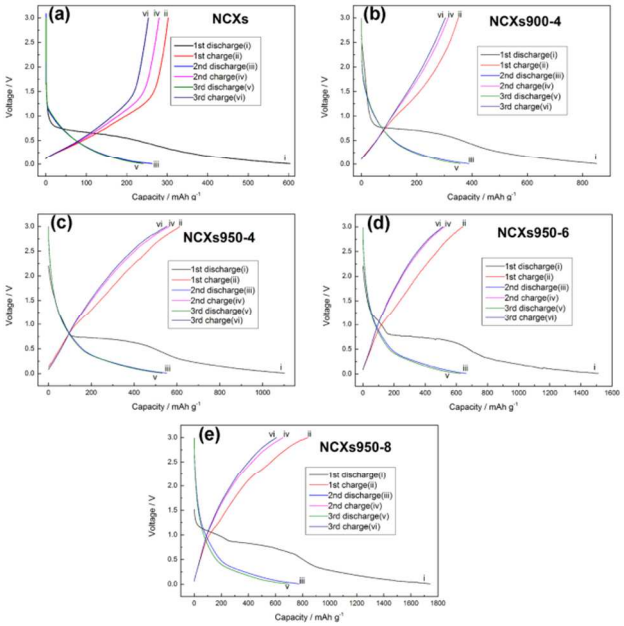

Fig. 6 Discharge/charge profiles of the multi-scaled porous NCXs.

The electrochemical properties of multi-scaled porous NCXs used as anode of lithium-ion battery are analysed in this section. Fig. 6 shows the charge/discharge profiles of the multi-scaled porous NCXs for the initial three cycles at a current density of 0.1C over a potential range of 0.01-3V. During the first discharge process of all samples, the voltage dropped rapidly and formed a plateau at about 0.75 V, which was observed only in the first cycle. This indicates the formation of a solid electrolyte interface (SEI) layer on the relatively large specific surface area of the sample.[34-36] The other plateau at about 0.1 V can be attributed to the intercalation of lithium ions in carbon xerogels materials.[34, 37] Our results and interpretations are consistent with those previous reports that large irreversible capacity observed in the first cycle is an unavoidable phenomenon in porous carbonaceous electrodes in lithium ion batteries. The phenomenon is generally ascribed to the formation of an SEI layer at the surface of porous carbon caused by reduction of the electrolyte and/or by irreversible lithium insertion into special positions in the vicinity of residual H atoms in the porous carbon.[38-41] In the cycles beyond the initial ones, all samples exhibited stable reversible capacities. It is also interesting to note that all activated samples have reversible capacities even higher than the theoretical capacity of graphite. This high capacity existing in activated NCXs cannot be explained simply by the conventional graphite intercalation mechanism.[38, 42, 43]

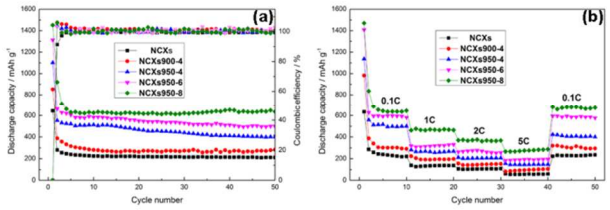

Fig. 7 The cycling performance and rate capability of the multi-scaled porous NCXs.

To analyse the stability of these NCXs, we conducted cycling measurements at a current density of 0.1C in the range of 0.01-3.0 V. The results are shown in Fig. 7a. After three cycles, the NCXs sample without activation displays very stable discharge capacities of 215 mAh g^{-1} up to 50 cycles. In comparison, activated NCXs all have higher discharge capacity and acceptable cycle ability. For example, the discharge capacity of NCXs900-4 (NCXs activated at 900^o C for 4 hours) is about 280 mAh g^{-1} after 50 cycles, with very good cycle stability. The NCXs sample activated at 950°C for 4 hours (NCXs950-4) shows yet even better discharge capacity than NCXs900-4. Among all NCXs, the NCXs sample having the longest activation duration at the highest activation temperature in this work, which is the sample activated at 950°C for 8 hours, shows the best specific capacity and cycle ability. Its discharge capacity is 645 mAh g^{-1} after 50 cycles, and the cycling performance is excellent.

Fig. 7b shows measured capacities at various charge/discharge rates of the multi-scaled porous NCXs. In such a test, the cell was first discharged/charged at a current density of 0.1C for 10 cycles, and then at various current densities of 1C, 2C, 5C and 0.1C for 10 cycles. As shown in Fig. 7b, the NCXs sample without activation exhibits only a slight capacity decrease even at high current density and present good cycle ability during the discharge/charge process. When the current density is increased from 0.1C to 1C, the reversible capacities of activated NCXs display a palpable decrease, which should be attributed to the existence of more micropores in activated NCXs and more intercalation of irreversible lithium ions in activated NCXs. Not surprisingly, the reversible capacities of activated materials are

still higher than the NCXs without activated. Notably, the NCXs950-8 anode still shows high lithium-ion storage and excellent cycling stability even at high rates. The reversible capacities were 645, 485, 390, 280, and 665 mAh g^{-1} for the sequential cycles with varying current density of 0.1C, 1C, 2C, 5C and 0.1C, respectively. Even at an extremely high current density of 5C (1860 mA g^{-1}), the reversible capacity is still 280 mAh g^{-1}, which is about 75% of the theoretical capacity of graphite. When the rate is tuned back to 0.1C after cycling at different rates, the specific capacity can be recovered to 665 mAh g^{-1}, which shows very stable cycling performance.

Other electrochemical properties such as charge/discharge capacity, cycle performance and rate capability of the CXs and activated products (CXs950-4) without nitrogen-doping are presented in Fig. S4, S5. These results indicate that for the same activation condition, nitrogen-doped NCXs consistently exhibit better electrochemical properties such as specific capacity and rate capacity than their CXs counterparts. Hence, nitrogen-doping is important.

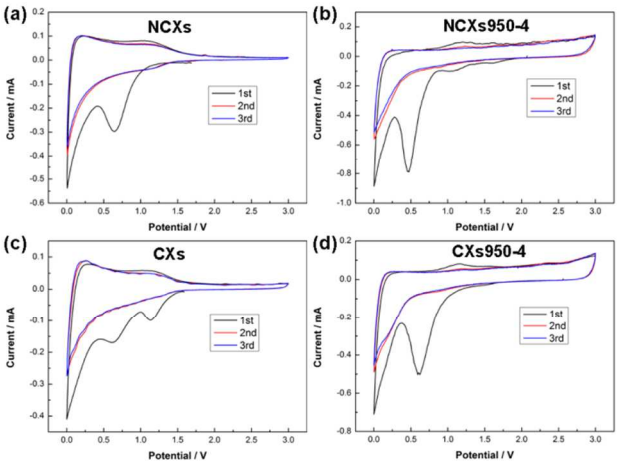

Fig. 8 Cyclic voltammetry curves of NCXs and CXs.

To track the relevant electrochemical processes, we recorded the CV profiles of the CXs and NCXs in the first three cycles (Fig. 8). The results of the CV profiles are in good agreement with the discharge-charge profiles. The CV curve of NCXs (Fig. 8a) exhibits two apparent peaks at 0.5-0.7 V and 0.01-0.2 V in the first discharge cycle. The first peak, which only appears in the first discharge cycle, can be attributed to the formation of an SEI film and the decomposition of electrolyte. The 0.01-0.2 V peak corresponds to the reversible insertion of lithium ions into graphite layers and structural defects in the electrode. The two broad peaks in the first charge cycle at about 0.2-0.8 V and 1.0-1.5 V are attributed to lithium ions extraction from the NCXs, which is in good agreement with previous reports on this topic.[27, 44-46] The first cycle CV curve of NCXs950-4 (activation at 950°C for 4 hours) (Fig 8b) is similar to the aforementioned CV curve of NCXs (Fig. 8a). Hence, the electrochemical processes and performance of these two samples are similar, with the exception that a difference between NCXs and NCXs950-4 is detected in the high potential regime of 1.3-3 V. In this regime, the CV curve of NCXs950-4 exhibits a feature with a rectangular shape. This feature is ascribed to capacitive lithium storage because many micro-pores/defects are created in the activation process and these may act as reservoirs for storage of lithium ions.[38] These electrochemical processes of NCXs950-4 are consistent with those of the NCXs950-6 and NCXs950-8 samples shown in Fig. S6. Moreover, compared with the second and third cycles of the CV curves, no significant curve shift is observed for both the NCXs and the activated samples. This implies that they have good cycling performance.

Combining the cycle performance test and rate capability (Fig. 7) reveals that the NCXs950-6 and NCXs950-8 samples exhibit more stable electrochemical performance than the other activated NCXs after 50 cycles, which could not be attributed to the porous structure, but to the nitrogen species of high quaternary-N content (Table 3) that exist in NCXs. This investigation shows that quaternary-N atoms seem to be the most important species for the reversible lithium ions storage in NCXs.

The electrochemical processes of CXs (Fig. 8c) and CXs950-4 (Fig. 8d) are similar to those of the NCXs and NCXs950-4 respectively except that the CV curve of CXs exhibits an additional apparent peak at 1.1-1.3 V in the first discharge process, which also can be attributed to the formation of SEI film and the decomposition of electrolyte.[45]

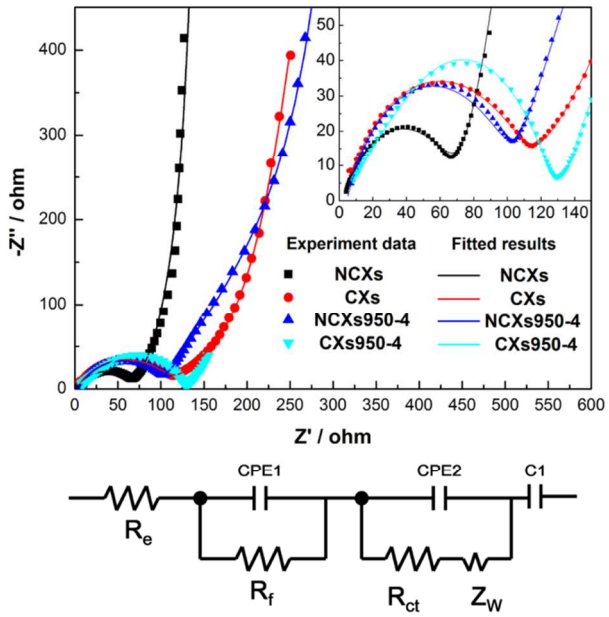

Fig. 9 Nyquist plots of the NCXs and CXs.

Table 4 Kinetic parameters of the NCXs and CXs.

Sample	R_e (ohm)	R_f (ohm)	R_{ct} (ohm)
NCXs	1.8	49.2	16.9
CXs	2.0	54.7	135.0
NCXs950-4	2.6	79.9	113.8
CXs950-4	3.2	88.5	249.7

The fitting values are derived from equivalent circuit.

The interconnected pores of the hierarchical porous NCXs provide fast paths for lithium ion transportation in materials and large surface area for the charge transfer of lithium insertion/extraction reaction; these are the important factors for improving rate capability.[47] The exceptional transport kinetics of lithium ion can be revealed by the EIS measurement. As shown in Fig.9, the Nyquist plots for NCXs and CXs consist of a depressed

semicircle in the high and middle frequency regions and a straight line in the low frequency region. In the equivalent circuit, R_e is the total resistance of electrolyte, electrode and separator, CPE1 and R_f are the surface film capacitance and the resistance for lithium ion migration through the SEI film, respectively. In addition, CPE2 and R_{ct} are the double layer capacitance and charge transfer resistance, respectively; Z_w is the Warburg impedance related to the lithium ions diffusion in the inserted materials; and C1 is related to insertion capacitance reflecting the occupation of lithium into the inserted sites.[47-49] The fitting values from this equivalent circuit are presented in Table 4. It can be seen that the composite resistance values of $R_{ct}+R_f$ which determine the charge transfer process of lithium ions insertion/extraction reaction, are 66.1 ohm and 189.7 ohm for the NCXs and CXs samples, respectively. The results confirm that nitrogen-doping can improve a carbon xerogel anode with higher conductivity. In analysis of the effects of CO_2 activation, the respective resistance ($R_{ct}+R_f$) values are 193.7 ohm and 338.2 ohm for NCXs950-4 and CXs950-4. Again, this confirms that nitrogen-containing NCXs950-4 has higher conductivity and faster transfer process than CXs950-4.

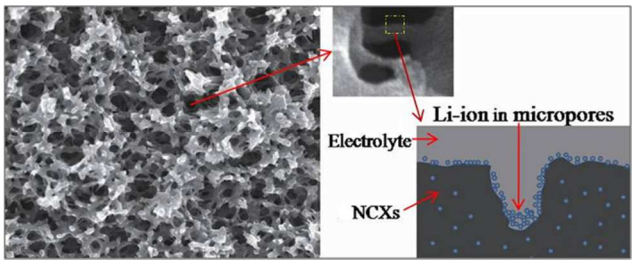

Scheme 2 Schematic representation of Li-ion storage in acvtivated NCXs.

The excellent capacity and rate capability of our carbon xerogels can be attributed to the novel porous nanostructure and nitrogen doping. As discussed above, the etching effect during the activation produces micro-/meso-pores. As illustrated in Scheme 2, the carbon xerogel framework provides conductive path for electron transportation. The large surface area leads to sufficient electrode and electrolyte interface to absorb lithium-ions. This promotes rapid charge transfer reactions. The micro-/meso-pores supply facile storage and transport channels for lithium-ions.[38, 43-45] Further, nitrogen-doping yields a large number of structural defects that promote rapid charge-transfer reactions and act as lithium insertion sites for storage of lithium-ion when the nitrogen-doped xerogel employed as an anode material in lithium ion battery. The results and interpretations are consistent with those in the literature.[50-53]

Finally, we note that the detailed analysis of the chemical states of nitrogen incorporated into all nitrogen-doped carbon xerogels shows a consistent trend of increasing relative concentration of quaternary-N, in the expenses of decreasing relative concentration of pyridinic-N and pyrrolic-N, when the temperature of CO_2 activation or the activation duration is raised. Accompanying this trend is the trend of improvements in all electrochemical properties when these NCXs are used as anode of lithium ion battery. This correlation implies that the presence of quaternary-N can improve anode performance in lithium ion battery. In fact, among all three nitrogen chemical states present in NCXs, quaternary-N is the only chemical state with which an incorporation nitrogen atom substitutes a carbon atom in the lattice of a perfect graphitic sheet. The lattice site substitution of a carbon atom with four valence electrons by a nitrogen atom with five valence electrons makes the lattice electron rich. As such, the lattice has higher conductivity and has an enhanced affinity to attract and accommodate lithium ions. In addition, the substitution of a carbon lattice site with a nitrogen atom will also distort the originally planar lattice structure. As such, when two nitrogen-doped graphitic layers are stacked, the layers cannot be stacked as perfectly as graphitic layers with no nitrogen-doping, and the interlayer distance of nitrogen-doped layers will also be slightly larger than the counterpart with no nitrogen-doping. These two differences both favour lithium intercalation and diffusion.

If our hypothesis and interpretation of quaternary-N being effective in improving anode performance in lithium battery is correct, we would have discovered a strategy for developing high-performance lithium battery. Interestingly, quaternary-N has also been found useful in enhancing oxygen reduction reactions and in developing high-performance fuel cells.[16] As such, the development of new methods for specific nitrogen-doping with the preferential formation of quaternary-N, in the expenses of decreasing the relative concentrations of other chemical states of nitrogen, should be intensified.

Conclusions

In conclusion, nitrogen-doped carbonaceous materials with hierarchical multi-scaled porosity is designed and demonstrated to possess abundant micro-/meso-pores, with an average pore size of about 2nm, which are well connected with percolated hallow-channels of about a micron in size. The good performance and a very high surface area of near 3000 $m^2 g^{-1}$ are well correlated to the coherent design and fabrication of hierarchical multi-scaled porosity. Lithium ion batteries with their anodes fabricated by these nitrogen-doped carbon xerogel materials show good improvements in all electrochemical performance, improvements which correlate well with both our nitrogen-doping method and our multi-scaled porosity design. Among all nitrogen-doped carbon xerogel materials prepared in this work, the sample fabricated with a melamine-resorcinol-formaldehyde gel as an xerogel precursor and with a pore-refinement step of CO_2 activation at 950°C for 8 hours show the best set of properties: specific surface area of 2912 $m^2 g^{-1}$, specific capacity of 645 mAh g^{-1} at 0.1C and 280 mAh g^{-1} even at 5C, good rate capability, and good cycle ability. More importantly, our chemical state analysis confirms that nitrogen is introduced into the carbon xerogels, with quaternary-nitrogen being the main chemical state of nitrogen correlating with our measurements of enhanced anode performance in lithium battery. Therefore, this work not only reveals a novel method for the preparation of nitrogen-doped carbonaceous materials with hierarchical multi-scaled porosity suitable for high-performance anodes of lithium batteries but also points out the importance of quaternary-nitrogen in the development of high-performance lithium batteries.

Acknowledgements

We thank the National High Technology Research and Development Program of China (863 Program) (2013AA050905), the Science and Technology Foundation of China Academy of Engineering Physics (No. 2012B0302041 and No.2013A0302014) for their financial support. We are grateful to Margaret Yau, Ka-Wai Wong, Jiahui Lin and Jinwei Chen for their valuable discussions and assistance in measurements.

Notes and references

[a] *Chengdu Green Energy and Green Manufacturing Technology R&D Center, Chengdu Development Center of Science and Technology, China Academy of Engineering Physics, Chengdu, Sichuan. Fax: 86-28-67070129 Tel: 86-28-67076208 E-mail: mliuhao@gmail.com*

[b] *Beijing Computational Science Research Center, Beijing 100084*

1. C. Marino, L. Boulet, P. Gaveau, B. Fraisse and L. Monconduit, *J. Mater. Chem.*, 2012, **22**, 22713.
2. C. Chae, J. Kim, J. Kim, Y. Sun and J. Lee, *J. Mater. Chem.*, 2012, **22**, 17870.
3. X. Fang, J. Zang, X. Wang, M.-s. Zheng and N. Zheng, *J. Mater. Chem. A*, 2013.
4. C. Huang, Q. Zhang, T. Chou, C. Chen, D. Su and R. Doong, *ChemSusChem*, 2012, **5**, 563.
5. B. Girgis, I. El-Sherif, A. Attia and N. Fathy, *J. Non-cryst. Solids*, 2012, **358**, 741.
6. V. Watson, C. Nieto Delgado and B. Logan, *Environ. Sci. Technol.*, 2013.
7. S. Shen, T. Zhao, J. Xu and Y. Li, *Energy Environ. sci.*, 2011, **4**, 1428.
8. S. Al‐Muhtaseb and J. Ritter, *Adv. Mater.*, 2003, **15**, 101.
9. J. Xu, A. Wang and T. Zhang, *Carbon*, 2012, **50**, 1807.
10. M. Gutiérrez, F. Picó, F. Rubio, J. Manuel Amarilla, F. Javier Palomares, M. Ferrer, F. del Monte and J. M. Rojo, *J. Mater. Chem.*, 2009, **19**, 1236.
11. F. Sillars, S. Fletcher, M. Mirzaeian and P. Hall, *Energy Environ. sci.*, 2011, **4**, 695.
12. S. Ci, Z. Wen, J. Chen and Z. He, *Electrochem. Commun.*, 2012, **14**, 71.
13. A. Reddy, A. Srivastava, S. Gowda, H. Gullapalli, M. Dubey and P. Ajayan, *ACS Nano*, 2010, **4**, 6337.
14. P. Ayala, R. Arenal, M. Rümmeli, A. Rubio and T. Pichler, *Carbon*, 2010, **48**, 575.
15. Z. Wen, X. Wang, S. Mao, Z. Bo, H. Kim, S. Cui, G. Lu, X. Feng and J. Chen, *Adv. Mater.*, 2012, **24**, 5610.
16. D. Geng, Y. Chen, Y. Chen, Y. Li, R. Li, X. Sun, S. Ye and S. Knights, *Energy Environ. Sci.*, 2011, **4**, 760.
17. H. Zhong, H. Zhang, S. Liu, C. Deng and M. Wang, *ChemSusChem*, 2013, **6**, 807.
18. H. Jin, H. Zhang, H. Zhong and J. Zhang, *Energy Environ. sci.*, 2011, **4**, 3389.
19. N. Subramanian, X. Li, V. Nallathambi, S. Kumaraguru, H. Colon-Mercado, G. Wu, J. Lee and B. Popov, *J. Power Sources*, 2009, **188**, 38.
20. H. Zhou, S. Xu, H. Su, M. Wang, W. Qiao, L. Ling and D. Long, *Chem. Commun.*, 2013, **49**, 3763.
21. G. Ruben and R. Pekala, *J. Non-Cryst. Solids*, 1995, **186**, 219.
22. E. Raymundo-Pinero, D. Cazorla-Amoros, A. Linares-Solano, U. Wild and R. Schlögl, *Carbon*, 2002, **40**, 597.
23. K. Mortensen, *J. Phys.: Condens. Matter*, 1996, **8**, A103.
24. I. Goldmints, J. Holzwarth, K. Smith and T. Hatton, *Langmuir*, 1997, **13**, 6130.
25. C. Lin and J. Ritter, *Carbon*, 2000, **38**, 849.
26. Y. Chang, C. Wu and P. Wu, *J. Power Sources*, 2013, **223**, 147.
27. L. Ji and X. Zhang, *Nanotechnology*, 2009, **20**, 155705.
28. A. C. Ferrari, *Solid State Commun.*, 2007, **143**, 47.
29. W. Kiciński, M. Norek and M. Bystrzejewski, *J. Phys. Chem. Solids*, 2013, **74**, 101.
30. X. Wang, C. Liang and S. Dai, *Langmuir*, 2008, **24**, 7500.
31. D. Long, J. Zhang, J. Yang, Z. Hu, G. Cheng, X. Liu, R. Zhang, L. Zhan, W. Qiao and L. Ling, *Carbon*, 2008, **46**, 1259.
32. H. Liu, Y. Zhang, R. Li, X. Sun and H. Abou-Rachid, *J. Nanopart. Res.*, 2012, **14**.
33. P. Hernández-Fernández, M. Montiel, P. Ocón, J. de la Fuente, S. García-Rodríguez, S. Rojas and J. Fierro, *Appl. Catal., B: Environmental*, 2010, **99**, 343.
34. L. Bulusheva, A. Okotrub, A. Kurenya, H. Zhang, H. Zhang, X. Chen and H. Song, *Carbon*, 2011, **49**, 4013.
35. Y. Zhu, X. Xiang, E. Liu, Y. Wu, H. Xie, Z. Wu and Y. Tian, *Mater. Res. Bull.*, 2012, **47**, 2045.
36. X. Wang, J. Wang, H. Chang and Y. Zhang, *Adv. Funct. Mater.*, 2007, **17**, 3613.
37. W. Ren, D. Li, H. Liu, R. Mi, Y. Zhang and L. Dong, *Electrochim. Acta*, 2013, **105**, 75.
38. L. Qie, W. Chen, Z. Wang, Q. Shao, X. Li, L. Yuan, X. Hu, W. Zhang and Y. Huang, *Adv. Mater.*, 2012, **24**, 2047.
39. Y. Hu, P. Adelhelm, B. Smarsly, S. Hore, M. Antonietti and J. Maier, *Adv. Funct. Mater.*, 2007, **17**, 1873.
40. P. Adelhelm, Y. Hu, L. Chuenchom, M. Antonietti, B. Smarsly and J. Maier, *Adv. Mater.*, 2007, **19**, 4012.
41. S. Yang, X. Feng, S. Ivanovici and K. Müllen, *Angew. Chem. Int. Ed.*, 2010, **49**, 8408.
42. S. Yang, X. Feng, L. Zhi, Q. Cao, J. Maier and K. Müllen, *Adv. Mater.*, 2010, **22**, 838.
43. N. Kaskhedikar and J. Maier, *Adv. Mater.*, 2009, **21**, 2664.
44. X. Zhou, J. Tang, J. Yang, J. Xie and B. Huang, *J. Mater. Chem. A*, 2013, **1**, 5037.
45. R. Song, H. Song, J. Zhou, X. Chen, B. Wu and H. Yang, *J. Mater. Chem.*, 2012, **22**, 12369.
46. Z. Jiang, B. Pei and A. Manthiram, *J. Mater. Chem. A*, 2013, **1**, 7775.
47. J. Yi, X. Li, S. Hu, W. Li, L. Zhou, M. Xu, J. Lei and L. Hao, *J. Power Sources*, 2011, **196**, 6670.
48. D. Lu, W. Li, X. Zuo, Z. Yuan and Q. Huang, *J. Phys. Chem. C*, 2007, **111**, 12067.
49. K. Zhang, P. Han, L. Gu, L. Zhang, Z. Liu, Q. Kong, C. Zhang, S. Dong, Z. Zhang, J. Yao, H. Xu, G. Cui and L. Chen, *ACS Appl. Mater. Interfaces*, 2012, **4**, 658.
50. J. Machnikowski, B. Grzyb, J. Weber, E. Frackowiak, J. Rouzaud and F. Béguin, *Electrochim. Acta*, 2004, **49**, 423.
51. H. Wang, C. Zhang, Z. Liu, L. Wang, P. Han, H. Xu, K. Zhang, S. Dong, J. Yao and G. Cui, *J. Mater. Chem.*, 2011, **21**, 5430.
52. W. Shin, H. Jeong, B. Kim, J. Kang and J. Choi, *Nano Lett.*, 2012, **12**, 2283.
53. X. Wang, Q. Weng, X. Liu, X. Wang, D. Tang, W. Tian, C. Zhang, W. Yi, D. Liu, Y. Bando and D. Golberg, *Nano Lett.*, 2014, **14**, 1164.

Graphical Abstract

Novel multi-scaled porous nitrogen-doped carbon is synthesized by enriching the simple resorcinol-formaldehyde method with: (a) addition of melamine for nitrogen-doping and micron-duct formation; (b) incorporation of PEO-PPO-PEO micelles for the optimization of the duct percolation; and (c) integration of CO_2 activation process for the most critical formation of abundant 2nm-pores. And their lithium storage performance is investigated.